Modeling and Prediction of Low-Frequency Near-Field Radiation for a Power Converter Based on the Operating Principle of a Monopole Antenna

Yirui Yang, *Student Member, IEEE*, Yanwen Lai, *Student Member, IEEE*, Shuo Wang, *Fellow, IEEE*,
and Zheng Luo

***Abstract*—This article develops a model to predict the measured near-field radiation via a monopole antenna based on the test setups specified by the EMI standards such as CISPR 25, DO-160E, MIL-STD-461E. The article first identified a major near-field radiation source in a dc–dc power converter. The operation principle of the monopole antenna is then studied, and a model is developed to predict the output voltage of the antenna. Next, the transmission line effect in the EMI test setup is identified and its impact on the measured radiated EMI is modeled. A prediction technique is developed for the low-frequency near-field radiation. Finally, experiments validated the developed theory.**

***Index Terms*—Electromagnetic interference (EMI), monopole antenna, near-field radiation, radiated emission.**

I. Introduction

WITH the development of high-speed semiconductor devices such as wide bandgap devices in modern power electronics, switching frequencies have been increased to reduce the size of passive components for high power densities [1], [2]. However, high switching frequencies lead to high radiated electromagnetic interference (EMI) even in the low-frequency range from 150 kHz to 30 MHz. EMI standards such as CISPR 25, DO-160E, and MIL-STD-461E, specify the radiated EMI limits and measurement setups from 150 kHz to 30 MHz. The radiated EMI from 150 kHz to 30 MHz has not been well understood and there is no enough existing literature addressing it. It is, therefore, necessary to develop a model to characterize and predict the radiated EMI at low frequencies.

The existing papers focused on developing radiation models for the EMI from 30 MHz to 1 GHz emitted from power cables measured with a log-periodic/biconical hybrid antenna [3], [4]. However, the radiated EMI from the components of a power converter was rarely investigated. In the case when the radiation from the components in the power converter is dominant, the models cannot predict the radiated EMI. Furthermore, the impact of the operating principle of the monopole antenna on the measured results is unknown. A theory to model and predict the radiated EMI from 150 kHz to 30 MHz should be developed.

In the cases where the radiation from the input and output cables of a converter is dominant, the existing literature focuses on the relationship between switching voltages, the common-mode (CM) excitation voltages applied across the input and output cables (antenna), and the measured radiated EMI via an antenna. The radiated EMI issues are generally addressed in studies [5] for nonisolated converters and [6] for isolated converters. Power converters, which act as CM noise sources for radiation, are modeled by applying the Thevenin equivalence at their input and output ports [7]. The excitation voltages in nonisolated converters are mainly the voltage drops of switching currents on the parasitic impedance of a ground layer [4], [8]. In isolated converters, the excitation voltages also include the unbalanced CM impedance of a transformer [6], [9]. Cables, an undesired radiation antenna, are primarily modeled with extracted gains from CM voltage [12] or CM current [11] to the measured radiated EMI. These gains are usually expressed in scattering parameters [10] or transfer functions [11]. The techniques to derive these gains include experimental extractions [10], [11], [12] and theoretical calculations based on the dipole antenna model [13], [14]. Different techniques to reduce radiated EMI have been proposed in the article [3], which include printed circuit board (PCB) layout optimization [8], [15], a cross-capacitor implementation [8], and the CM inductor and Y-capacitor design [16]. The radiated EMI has not been sufficiently modeled from an electromagnetic field perspective.

Regarding the radiated EMI, in the low frequency (LF) range (150 kHz–30 MHz), due to the long wavelength (>10 m), for the measurement with a monopole (rod) antenna 1 m away from the converter as specified in EMI standards, the measured is near electric field. The near electric field due to the voltage pulsating components in the converter could be a major source of the measured EMI. Some existing works have explored the near field of devices other than the cables, such as the PCB traces [17], IGBT modules [18], commutation loops [19], and wireless charging coils [20]. Some research revealed that the LF radiated EMI was dominated by the near electric field emitted from the

---

Manuscript received 4 April 2024; revised 1 July 2024; accepted 5 August 2024. Date of publication 12 August 2024; date of current version 11 September 2024. This work was supported by Monolithic Power Systems, Inc. Recommended for publication by Associate Editor F. Leferink. *(Corresponding author: Shuo Wang.)*

Yirui Yang, Yanwen Lai, and Shuo Wang are with the Department of Electrical and Computer Engineering, University of Florida, Gainesville, FL 32611 USA (e-mail: yirui.yang@ufl.edu; shuowang@ieee.org).

Zheng Luo is with the Monolithic Power Systems, Inc., San Jose, CA 95119 USA (e-mail: zheng.luo@monolithicpower.com).

Color versions of one or more figures in this article are available at https://doi.org/10.1109/TPEL.2024.3441810.

Digital Object Identifier 10.1109/TPEL.2024.3441810

power inductor instead of cables in a buck–boost converter [21], [22], [23].

For the radiated EMI measurement, Song et al. [24] revealed that the measurement was impacted by the receivers, preamplifiers, and connectors in the setups. Some studies have included information on test setups other than cables in their models [25]. Qiang and Yinghua [26] disclosed that the measurement was very sensitive to the antenna types, directivity, and phase center. Therefore, there has been exploration into including antennas in simulation models for more accurate predictions [27], [28], as well as attempts to use analytical methods for antenna gain calculation [29]. The antenna gain and phase center were used to characterize the antenna's output voltage for far-field electric field. As the phase center and antenna gain are calibrated in the far-field context, they are invalid for near electric field analysis. To overcome this barrier, investigating the operating principle of monopole antenna in near electric field measurement is necessary to accurately predict the measured LF radiated EMI.

For the LF-radiated EMI test setups in CISPR 25, DO-160E, and MIL-STD-461E, the measurement is impacted by the resonance due to the structure of the measurement setups [30], [31]. Existing papers focused on developing techniques to reduce the impact of the resonance [32], [33]. However, resonance is an intrinsic characteristic of the measurement setups, so to accurately predict the measured EMI, the radiated EMI under the influence of the resonance should be modeled.

The contributions of this article include the following.

1) A theory was developed and quantified to predict the output voltage of a monopole antenna under the near-field condition instead of a plane wave assumption. It is valid for LF near-field radiation measurements.
2) The impact of transmission line effect of the measurement setup was studied for CISPR 25. The mechanism was revealed and a technique to quantify the impact was developed to predict the measured EMI.
3) Radiation models for three power converters were developed to predict the LF radiated EMI, and they were validated with the measurements.

The rest of this article is organized as follows. In Section II, a power inductor is identified as a major source for the LF radiated EMI under the setup of CISPR 25. In Section III, the operating principle of a monopole antenna is studied and a model is developed to predict the measured near electric field EMI. The developed model is further validated with experiments. In Section IV, the impact of measurement setup in CISPR 25 is studied. A technique to model the impact of transmission line effect is developed and verified. Finally, Section V concludes this article.

II. POWER INDUCTOR AS THE RADIATION SOURCE

A. Converter Under the CISPR 25 Test Setup

A buck–boost converter, which is used as an automotive LED driver, will be studied in this article. Fig. 1 is the schematic of the converter. Both input and output voltages are 12 V. The load is four series LED light bulbs with a load current 1.2 A. The converter's switching frequency is 1 MHz. The inductor L has an inductance of 4.7 μH. The MOSFET SW and the diode D are integrated into the power IC MPQ7200, a single-chip power module manufactured by Monolithic Power Systems, Inc.

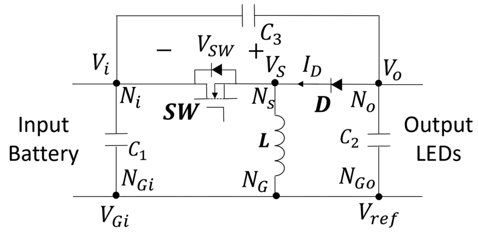

Fig. 1. Schematic of the buck–boost converter under investigation.

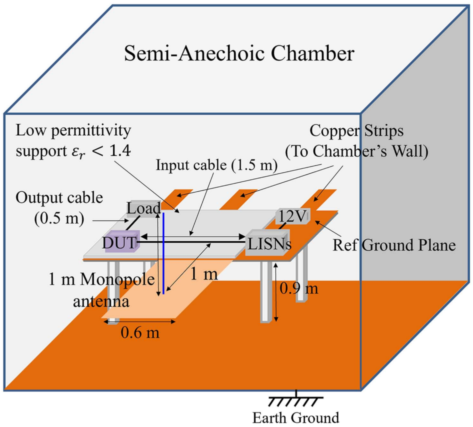

Fig. 2. Test setup specified in CISPR 25 for electric field measurement (150 kHz–30 MHz).

According to the CISPR 25, a test setup in Fig. 2 is used to measure the radiated EMI from 150 kHz to 30 MHz. In this setup, the converter has a 1.5-m input power cable and a 0.5-m output power cable. The input cable connects the converter to a 12-V battery. The output cable connects the converter to the load. Two line impedance stabilization networks (LISNs) are inserted between the battery and the input cable to isolate the battery from the EMI measurement. The EMI measurement was conducted in a 3-m semianechoic chamber. The copper tabletop is grounded to the chamber's walls with copper strips as a reference plane. The converter and the cables are 5 cm above the reference ground plane. A 1.04-m long monopole antenna is used to measure electric field.

B. Identify the Inductor As the Major Source of Radiated EMI

In the existing literature, the radiated EMI model was developed in Fig. 3. The input and output cables were modeled as a dipole antenna with antenna impedance $R_L + R_r + jX_A$. Based on Thevenin equivalence, the converter was modeled as a CM noise voltage source V_{CM} in series with a CM impedance Z_{CM}. The switching operation of the converter leads to excitation voltage V_A across the antenna, resulting in CM current I_{CM} for the radiation. With this model, the antenna's transfer gain from V_A to the measured EMI can be further derived based on the experiments. This gain is independent of the converter and is a

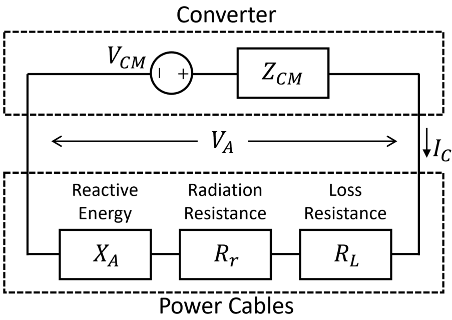

Fig. 3. Radiated EMI model based on the assumption that the cable contributes to the dominant part in the measured EMI.

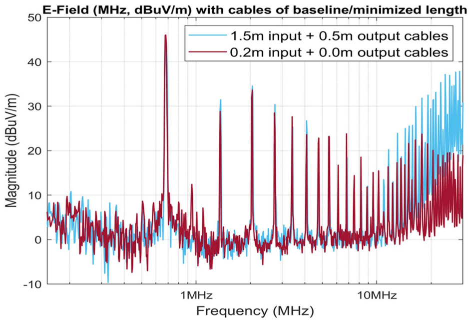

Fig. 4. High radiated EMI at LFs was not due to cables below 10 MHz.

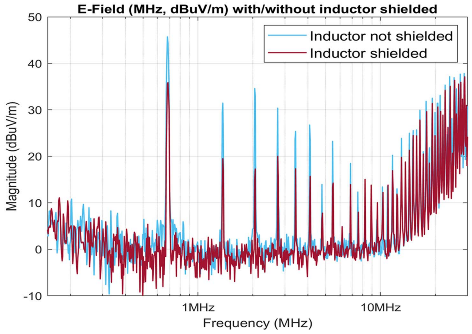

Fig. 5. Inductor is the major source of the radiated EMI below 10 MHz.

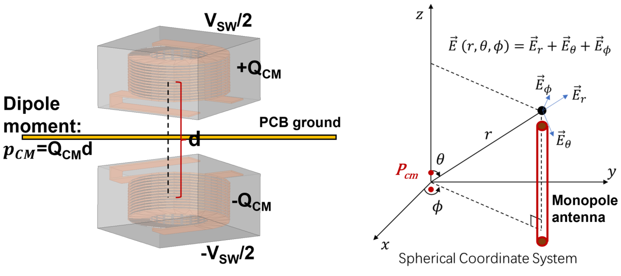

(a) (b)

Fig. 6. (a) Inductor electric dipole moment $p_{\rm CM}$ due to the CM voltage $\rm V_{SW}/2$. (b) Electric field due to $p_{\rm CM}$ in a spherical coordinate system with a monopole antenna.

function of the test setup only. This derivation avoids developing the model to predict the transfer function from V_A to the near electric field launched to the antenna and the model to predict the transfer function from the electric field to the output voltage of the antenna.

However, if the converter and cables have been optimized to minimize V_A and the CM current $I_{\rm CM}$ on the cables, other radiation mechanisms could be dominant, so the model may not be able to predict the radiated EMI anymore.

As analyzed in [8] and [15], $V_{\rm CM}$ in Fig. 3 was due to the voltage drops of switching currents on critical parasitic impedances across the input and output cables, which includes the PCB ground impedance between nodes $\rm N_{Gi}$ and $\rm N_{Go}$ and the impedances of capacitor $\rm C_1$ and $\rm C_2$ in Fig. 1. For the converter under investigation, the PCB ground and capacitor impedances have been significantly reduced by the optimal design so V_A is very small, and the cables' radiation can be ignored at LFs.

To identify the major radiated EMI source at LFs, two tests were conducted. In the first test, the input and output cable lengths were reduced from 1.5 m and 0.5 m to 0.2 m and 0 m, respectively. The measured radiated EMI is compared in Fig. 4. Based on antenna theory, because the wavelength is much larger than the cable lengths, the radiated EMI should be decreased after the cable length is reduced [8]. In Fig. 4, the measured EMI below 10 MHz almost has no any changes, which indicates that the cable's radiation is not dominant below 10 MHz. In the second test, the inductor in the converter was electrically shielded and the shielding was grounded to the $\rm N_G$ node in Fig. 1. The cable lengths were not changed in this test. The measured radiated EMI with the shielding is up to 18 dB (87%) lower than that without shielding below 10 MHz in Fig. 5. Therefore, the inductor is the dominant contributor to the LF radiated EMI.

In [23], the mechanism of the radiation due to a surface mount power inductor in a buck–boost converter was investigated. In Fig. 1, the switching voltage V_{SW} across the MOSFET leads to the same amount of switching voltage added to the inductor L. This voltage can be decomposed into DM voltage (-V_{SW}/2, V_{SW}/2) and CM voltage V_{SW}/2 with the voltage at $\rm N_G$ on the PCB ground plane as the reference. It has been presented in [23] that the radiated near electric field can be predicted based on the electric dipole moment theory. The inductor carries DM and CM charges due to the decomposed DM and CM voltages and the DM and CM parasitic capacitances to the reference ground. The DM charges mostly concentrate on the two ends close to the first and last winding turn of the inductor and the CM charge $\rm Q_{CM}$ exists on the surface of the whole inductor. Based on the image theory, both DM and CM charges have images under the reference PCB ground at the same distance to the ground as that of the DM and CM charges above the PCB ground, respectively. The charges and their images form DM and CM electric dipole moments. It has been proved in [23] that the near electric field radiated from the CM dipole moment $p_{\rm CM}=Q_{\rm CM}d$ due to CM charge is dominant, as in Fig. 6(a), so the contribution from the DM charge is ignored here.

The near electric field emission from an inductor, which is vertically mounted on the PCB ground plane, due to its CM charge is derived in [23] in a spherical coordinate system (r,θ,φ), as in Fig. 6(b)

$$\begin{cases} E_r = \frac{p_{CM} cos\theta}{2\pi\varepsilon_0 r^3} \\ E_\theta = \frac{p_{CM} sin\theta}{4\pi\varepsilon_0 r^3} \\ E_\varphi = 0 \end{cases} . \tag{1}$$

In (1), the origin of the spherical coordinate is at the center of the electric dipole.

The near electric field will induce a voltage at the output of the antenna in Fig. 2. The existing technique calibrates the monopole antenna under far field, so the results cannot be applied to the near field measurements. The mechanism of the induced voltage due to near electric field must be investigated.

III. EFFECTIVE E-FIELD THEORY FOR MONOPOLE ANTENNA

The relationship between the output voltage of a monopole antenna and the strength of the measured uniform E field has been analyzed in antenna theory textbooks. The brief conclusion is that a monopole antenna is vertically polarized and only responds to the vertical component of the E field.

However, it is important to note that the conclusions in antenna theory textbooks are derived under an emphasized assumption: the transmitting and receiving antennas are far apart, and the EM waves reaching the receiving antenna are uniform planar waves. This assumption is natural and common in communication scenarios. In contrast, in the CISPR 25 test setup here, the equipment under test (EUT) and the receiving antenna are within each other's near-field range. As a result, the E field reaching the receiving antenna is nonuniform in either intensity or direction. In such cases, directly applying the conclusions from antenna theory is not rigorous. Therefore, this section develops a receiving antenna model suitable for LF EMI testing environments.

A. Antenna Factor Under Standard Conditions

The monopole (rod) antenna used in the test is VAMP 9243 manufactured by Schwarzbeck. This antenna is designed to measure a vertically polarized electromagnetic wave within the frequency range of 9 kHz to 30 MHz. It has a vertical aluminum rod of 1 m in length with 8-mm radius. The rod is installed on a grounded 0.6 m × 0.6 m aluminum counterpoise. The rod and the counterpoise are isolated at the bottom of the rod with a gap, as in Fig. 7(a). The voltage across the gap is V_{gap}. V_{gap} is the induced voltage on the antenna due to the electric field in the air. V_{gap} is further amplified by an active amplifier installed under the counterpoise. The amplifier has a very high input impedance, and a 50-Ω output impedance.

For an incident plane wave whose propagation direction is orthogonal to the rod, its electric field intensity $E_{inc,dB}$ in dB(μV/m) is vertically polarized, as in Fig. 7(a). In this case, the antenna's final output voltage V_{out} in dB(μV) at the output of the amplifier is proportional to the intensity of incident wave. Therefore, in a log scale, antenna factor $F_{a,dB}$ in dB/m, is defined in

$$F_{a,dB} = E_{inc,dB} - V_{out,dB}. \tag{2}$$

$F_{a,dB}$ is usually provided in the antenna's manuals.

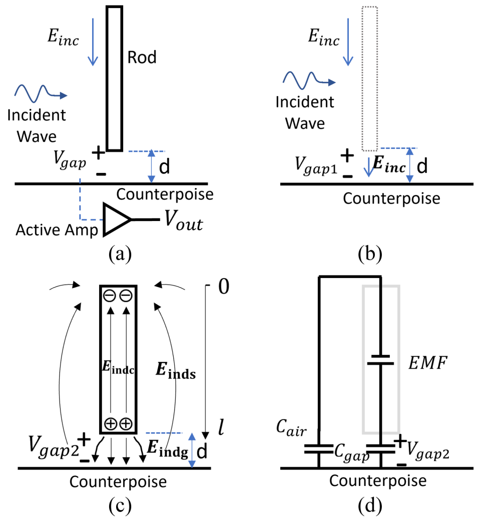

Fig. 7. Interaction between a monopole and the electric field of an orthogonal incident plane wave. (a) Monopole antenna and an orthogonal incident wave. (b) Incident electric field's contribution $V_{\text{gap}\ 1}$ to V_{gap}. (c) Induced charge on the rod and the counterpoise contributes V_{gap2} to V_{gap}. (d) Equivalent capacitance model.

Since the monopole antenna's dimensions are no more than 1/10 of the wavelength of the maximum concerned frequency (30 MHz), the phase shift along the antenna is ignored. The analysis can therefore be based on the electrostatic theorem. As shown in Fig. 7(a), the metal rod is illuminated by the external electric field E_{inc}. As a result, a voltage V_{gap} is induced across the gap between the rod and the counterpoise. V_{gap} is further amplified by the amplifier for an output voltage V_{out}. Therefore, (2) can be rewritten as

$$F_{a,dB} = (E_{inc,dB} - V_{\text{gap},dB}) + (V_{\text{gap},dB} - V_{\text{out},dB}). \tag{3}$$

In (3), ($E_{inc,dB}$-$V_{\text{gap},dB}$) represents the interaction between the rod antenna and the E field, and it depends on the antenna's physical structure. ($V_{\text{gap},dB}$-$V_{\text{out},dB}$) is the gain of the amplifier.

In Fig. 7(a), V_{gap} is equal to the integration of the electric field across the gap. Two sources contribute to the electric field in the gap. One is electric field intensity E_{inc} directly from the incident wave, as in Fig. 7(b). The other is E_{indg} across the gap due to the induced charges on the rod and the counterpoise, as shown in Fig. 7(c). In Fig. 7(c), the induced electric field is in three regions: E_{indg} in the gap, E_{indc} inside the antenna and E_{inds} outside the antenna and gap. Based on the superposition theorem, the V_{gap} can be decomposed into two parts as

$$\begin{aligned} V_{gap} &= V_{gap\ 1} + V_{gap\ 2} \\ V_{gap\ 1} &= E_{inc}\ \times d \\ V_{gap\ 2} &= E_{indg}\ \times d \end{aligned} \tag{4}$$

where V_{gap1} is the contribution from the incident wave; V_{gap2} is the contribution from the induced charges. As most of the induced charges concentrate on the two ends of the rod, strong E_{indg} is generated in the gap, which is much larger than E_{inc}. In a finite element analysis simulation (gap=5 mm), E_{indg} is more than 700 times higher than E_{inc}. Therefore, V_{gap2} is dominant in (4), so V_{gap1} is ignored in the following analysis.

As the rod is highly conductive, the total electric field intensity inside the rod is zero. In other words, the E_{indc} induced inside the antenna due to the charges at the two ends meet

$$E_{indc} + E_{inc} = 0. \tag{5}$$

Inside the gap and outside of the antenna and the gap, the relationship between the electric field and the voltages can be modeled as lumped capacitors, C_{gap} and C_{air}, respectively, as in Fig. 7(d). The induced charges in the rod result in an electromotive force (EMF) across the two ends. The EMF along the rod due to the induced charges is

$$EMF = -\int_0^{l_{rod}} \overrightarrow{E_{indc}} \cdot \overrightarrow{dl}. \tag{6}$$

The integration is along the rod from its top to bottom. The EMF results in V_{gap2} in (4). From (5) and (6)

$$EMF\ = E_{inc} \cdot l_{rod}. \tag{7}$$

In (7), l_{rod} is the length of the rod. From Fig. 7(d), V_{gap2} is

$$V_{\text{gap2}} = \frac{C_{air}}{C_{air} + C_{gap}} EMF = \frac{C_{air}}{C_{air} + C_{gap}} \cdot E_{inc} \cdot l_{rod}. \tag{8}$$

In (8), l_{rod}, C_{air}, and C_{gap} are constants determined by the dimensions and the setup of the antenna. Thus, V_{gap2} is proportional to E_{inc}. As $V_{\text{gap}} \approx V_{\text{gap2}}$, (8) can be rewritten in a log scale as (9), which is the first part of (3). Equation (9) reveals the relationship between the electric field of a plane wave and the gap voltage under ideal conditions

$$E_{inc,dB} - V_{gap,dB} = -\text{dB}\left(\frac{C_{air} \cdot l_{rod}}{C_{air} + C_{gap}}\right). \tag{9}$$

B. Derive Effective E-Field Measured in Practical Conditions

The actual monopole antenna's operating condition in Fig. 2 is different from the ideal condition discussed above. First, the incident wave's propagation direction is not orthogonal to the rod. Second, the electric field intensity is uneven along the rod.

The electric field of a general incident wave in Fig. 8(a) can be decomposed to two components: $E_{inc,xy}$ perpendicular to the rod and $E_{inc,z}$ in parallel with the rod.

In Fig. 7(b), $E_{inc,xy}$ will induce charges on the two sides of the rod. The electric field $E_{ind,xy}$ due to the induced charges has the same magnitude as but with reverse direction to $E_{inc,xy}$ inside the rod, so it cancels the $E_{inc,xy}$ inside the rod. As a result, the net electric field is zero inside the rod. The induced charge due to $E_{inc,xy}$ does not contribute to V_{gap} because $E_{ind,xy}$ is perpendicular to the integration path of electric field for V_{gap}.

The lumped model is shown in Fig. 8(c). emf_{xy} is the equivalent EMF due to $E_{inc,xy}$. Because of the horizontal symmetry of the structure, C_{gap} is not charged by emf_{xy}. In summary, both $E_{inc,xy}$ and $E_{ind,xy}$ do not contribute to V_{gap}.

On the other hand, like that in Fig. 7, $E_{inc,z}$ will induce charges on the top and bottom of the rod, and on the counterpoise. The charges will generate electric field inside the rod to cancel $E_{inc,z}$ so the net electric field inside the rod is zero. The lumped model is shown in Fig. 8(d). In Fig. 8(d), emf_z, given by in (10), is the equivalent EMF along the rod due to the induced charges. The integration path in (10) is from the top to the bottom within the rod

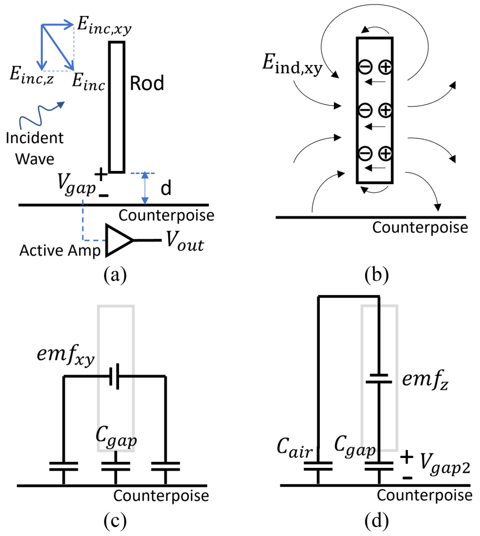

(a) (b)
(c) (d)

Fig. 8. Interaction between a monopole and an electric field in a nonideal condition. (a) Monopole antenna and an incident wave. (b) Charges induced by the incident electric field component orthogonal to the rod, and the resultant electric field. (c) Equivalent model for the charges induced by the incident electric field component orthogonal to the rod. (d) Equivalent model for the charges induced by incident electric field component parallel with the rod.

$$emf_z = \int_0^{l_{rod}} \overrightarrow{E_{inc,z}} \cdot \overrightarrow{dl}\ . \tag{10}$$

Like that in Fig. 7, V_{gap} is mainly contributed from the induced charges on the bottom and counterpoise, so $V_{\text{gap}} \approx V_{\text{gap2}}$. In the gap, if the electric field due to the induced charges is $E_{indg,z}$, $E_{indg,z}$ will dominate the electric field in the gap.

From (10), V_{gap2} with uneven $E_{inc,z}$ can be derived as

$$V_{\text{gap2}} = \frac{C_{air}}{C_{air} + C_{gap}} \int_0^{l_{rod}} \overrightarrow{E_{inc,z}} \cdot \overrightarrow{dl}. \tag{11}$$

The effective even electric field E_{eff} is defined as

$$E_{\text{eff}} = \frac{1}{l_{rod}} \int_0^{l_{rod}} \overrightarrow{E_{inc,z}} \cdot \overrightarrow{dl}. \tag{12}$$

From (12), the impact of uneven $E_{inc,z}$ can be represented with E_{eff}. Therefore, according to (2), the antenna's output voltage is

$$V_{out,dB} = \left[\frac{1}{l_{rod}} \int_0^{l_{rod}} \overrightarrow{E_{inc,z}} \cdot \overrightarrow{dl}\right]_{dB(\mu V/m)} - F_{a,dB}. \tag{13}$$

In (13), $F_{a,dB}$ is the antenna factor provided by manufacturers in dB/m and $V_{out,dB}$ is in dBμV.

With the help of (13), the output voltage of the monopole antenna in Fig. 2 can be predicted.

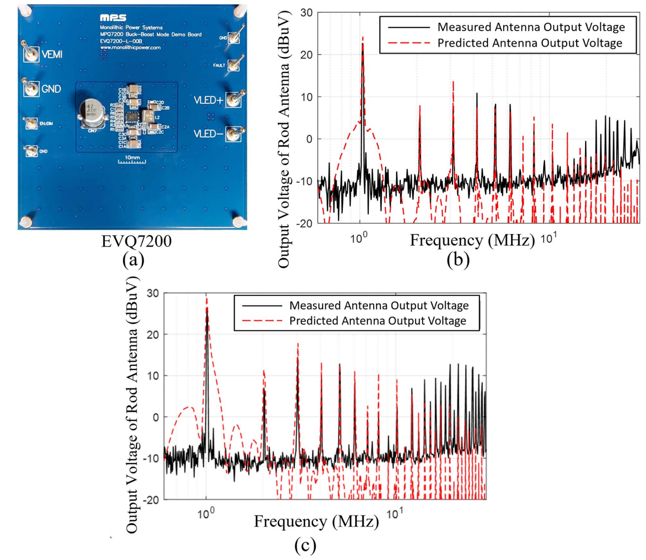

(a) (b) (c)

Fig. 9. Comparison of the predicted and measured EMI for the converter EVQ7200 with two different inductors. (a) EVQ7200 power converter. (b) EMI comparison between the predicted and measured for inductor Coilcraft XEL4030-472MEB. (c) EMI comparison between the predicted and measured for inductor MPS MPL-AL6050-4R7.

C. Verification With Experiments

To verify the proposed modeling technique, experiments were conducted in a CISPR 25 setup as in Fig. 2. Two converters: monolithic power systems (MPS) EVQ7200 and EVQ2483 evaluation boards, were tested in the experiments. The two converters have switching frequencies of 1 MHz and 700 kHz, respectively. Both the input and output voltages of the two converters are 12 V and 12 V. Both output currents are 1.2 A. The two power inductors used on EVQ7200 have an inductance of 4.7 μH with model numbers Coilcraft XEL4030-472MEB (volume: 4 $\times$ 4 $\times$ 2.9 mm^3) and MPS MPL-AL6050-4R7 (volume: 6 $\times$ 6 $\times$ 4 mm^3). The inductor used on EVQ2483 has an inductance of 10 μH with model number Toko DH124C-1010ASW-100M (volume: 12 $\times$ 12 $\times$ 4 mm^3). For both converters, the electric fields emitted from power inductors are dominant, as analyzed in Section II.

In the first experiment, the electric field distributions in the space along the rod antenna due to the inductor XEL4030-472MEB on the converter EVQ7200 in Fig. 9(a) was first predicted with the model developed in [23], as described in Section II. The output voltage of the antenna was then predicted using (13). The result was finally compared with the measured one with the setup in Fig. 2 in Fig. 9(b). They match well below 12 MHz. In the second experiment, the inductor on EVQ7200 was replaced with MPL-AL6050-4R7. The prediction and measurement were repeated as in the first experiment. The results were compared in Fig. 9(c). They also match well below 6 MHz with less than 3 dB difference.

The third experiment was conducted on converter EVQ2483 in Fig. 10(a). The spectra of the predicted and measured antenna output voltage were compared in Fig. 10(b). They match well below 6 MHz with less than 3 dB difference.

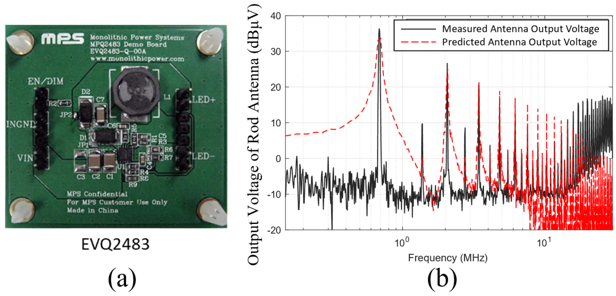

(a) (b)

Fig. 10. Comparison of the predicted and measured EMI for the converter EVQ2483. (a) EVQ2483 power converter. (b) EMI comparison between the predicted and measured.

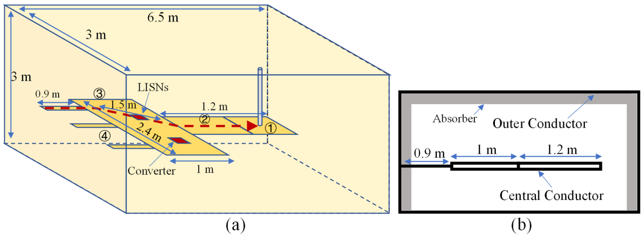

(a) (b)

Fig. 11. Characterize the measurement setup. (a) Measurement setup. (b) Simplified setup for analysis.

In both Figs. 9 and 10, for the frequencies above 6 MHz, the predicted is higher than the measured at frequencies around 10 MHz and lower than the measured above 13 MHz. The discrepancy has been identified due to the impact of the transmission line effect of the measurement setup.

IV. MEASUREMENT SETUP AND ITS IMPACT ON THE EMI

Based on CISPR 25, the EMI measurement should be conducted in a semianechoic chamber, as in Fig. 11(a). The four sidewalls and the ceiling of a semianechoic chamber are covered with electromagnetic (EM) absorbers and the floor of the chamber is a grounded copper plane without being covered by absorbers. The EM wave emitted from a source inside the chamber will have a reflection when it reaches any side of the chamber. The absorbers usually do not have good performance at low frequencies below 30 MHz, so they cannot significantly reduce the reflection. The EM wave has a bigger reflection on the floor than other sides covered with absorbers. The monopole antenna measures the total electric field including those directly emitted from the noise source and those reflected from the chamber sidewalls, ceiling, and floor.

A. Analysis of the Impact of Measurement Setup

It was found that the setup in Fig. 2 can be characterized by the model in Fig. 11. As shown in Fig. 11(a) and (b), the ceiling, floor, and sidewalls of the chamber perform like the outer conductor of a cavity. The central conductor consists of, ① the monopole antenna's counterpoise, ② the grounding connection, ③ reference ground plane on the table, and ④ the copper strips connecting reference ground plane to the chamber's grounded

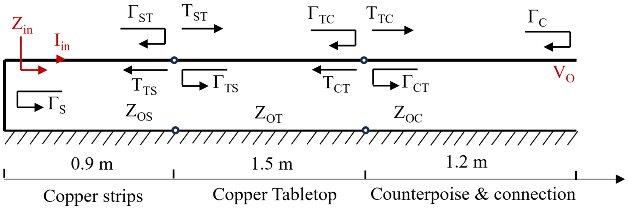

Fig. 12. Reflections and transmissions of the EM waves at the interfaces of counterpoise and connection, copper tabletop, copper stripes, and left and right ends along the transmission lines.

TABLE I

TRANSMISSION LINES' PER-UNIT-LENGTH PARAMETERS

Section	R (Ω/m)	L (H/m)	G (S/m)	C (F/m)
Copper strips	0.86×10^{-3}	218×10^{-9}	0	52×10^{-12}
Copper Tabletop	0.23×10^{-3}	171×10^{-9}	0	66×10^{-12}
Connection & counterpoise	0.58×10^{-3}	447×10^{-9}	0	25×10^{-12}

wall. In Fig. 11(b), the length of the copper tabletop is 1.5 m instead of the width 1 m of the tabletop because the converter is close to the side copper strip, which results in a longer current path from the grounded wall through the side strip to the ground connection ② approximately equal to 1.5 m. The right end of the central conductor is floating, and the left end is grounded to the chamber's ground. The total equivalent length from the right end to the left end is 3.6 m, as shown in Fig. 11(a) and (b).

If the six sides of the grounded chamber are taken as a voltage reference, conductor ① and ②, conductor ③, and conductor ④ are like 3 transmission lines cascaded with different characteristic impedances, as in Fig. 12. These transmission lines have characteristic impedance Z_{OC} for counterpoise and connection, Z_{OT} for copper tabletop, and Z_{OS} for copper strips, respectively. To determine these characteristic impedances, the per-unit-length parasitic parameters of the three transmission-line sections are extracted using the two-dimensional extractor function in Ansys Electronics' Q3D based on the dimensions of the cross-sectional view of each transmission-line section in the test setup. These parameters include the resistance R (in Ω/m), the inductance L (in H/m), the admittance G (in S/m), and the capacitance C (in F/m). The extracted per-unit-length parasitic parameters for each transmission-line section are in Table I.

It is shown in Table I that $R<<|j\omega L|$ and $G<<|j\omega C|$ between 150 kHz and 30 MHz. For the characteristic impedance Z_O of the transmission line

$$Z_{\mathrm{o}} = \sqrt{\frac{R+j\omega L}{G+j\omega C}}\,. \tag{14}$$

The characteristic impedances Z_{OC}, Z_{OT}, and Z_{OS} of the three transmission lines have angles less than 0.13° in the frequency range of 150 kHz–30 MHz. Therefore, they can be reasonably approximated as real numbers.

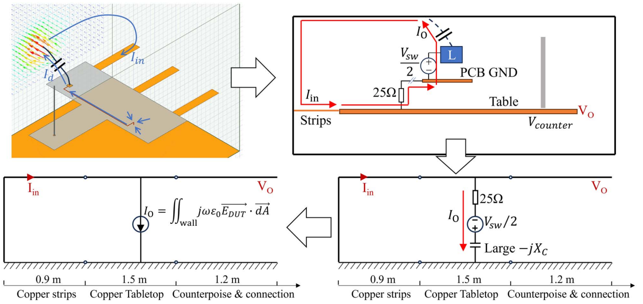

Fig. 13. Noise source for the displacement current flowing from the inductor to the walls of the chamber, to the central conductor and finally back to the inductor via 25 Ω (2 paralleled 50-Ω LISNs) can be characterized with an equivalent CM voltage source $V_{SW}/2$ in series with a source impedance jX_C.

In Fig. 12, based on transmission line theory, when an EM wave propagates along these three transmission lines, the reflections and transmissions happen at the interfaces, the right and left ends of the transmission lines. Based on transmission and reflection coefficients in (15) and (16), the transmission across the interface of two transmission lines will, therefore, not result in EM wave's phase change in Fig. 12. In (15) and (16), Γ_{xy} and T_{xy} are reflection and transmission coefficients when an EM wave flow from a transmission line with a characteristic impedance Z_{OX} to a transmission line with a characteristic impedance Z_{OY}, where $x \neq y$ and $x, y \in (C, S, T)$

$$\Gamma_{\mathrm{xy}} = \frac{Z_{\mathrm{Oy}} - Z_{\mathrm{Ox}}}{Z_{\mathrm{Ox}} + Z_{\mathrm{Oy}}} \tag{15}$$

$$T_{\mathrm{xy}} = \frac{2Z_{\mathrm{Oy}}}{Z_{\mathrm{Ox}} + Z_{\mathrm{Oy}}}\,. \tag{16}$$

Although the three transmission lines have different characteristic impedances, when EM waves propagate through the interfaces between two transmission lines, only magnitudes change, and phases do not change. Furthermore, At the left end, the reflection coefficient Γ_S = -1 and at the right end, the reflection coefficient $\Gamma_C = 1$.

In Fig. 13, due to the pulsating CM voltage $V_{SW}/2$ on the inductor, there is a displacement current flowing from the inductor to the side and top walls of the chamber via the equivalent capacitive reactance $-jX_C$. This CM noise current will flow back to the central conductor, LISNs, input cable harness, and finally back to the inductor. For this CM noise current, two 50-Ω LISNs are in parallel resulting in a 25-Ω resistance. The impedance of X_C, equivalent to a 0.3-pF capacitance per Ansys Q3D simulation, is much larger than the other impedances in the loop in the frequency range of interest. By modeling the CM voltage source as $V_{SW}/2$ in Fig. 13, a current source $I_O = j0.5V_{SW}/X_C$ provides a reasonable approximation of the noise source in Fig. 13.

In Fig. 14, the electric field measured by the monopole antenna is determined by not only the vertical electric field E_{DUT} directly from the power inductor, but also from E_{counter} due to the voltage V_{counter} of the counterpoise under the monopole antenna. The measured electric field is E_{DUT} - E_{counter}. It is thus necessary to investigate the voltage along the central conductor in Fig. 15.

In Fig. 15, the current source I_O is located Δl=0.9 m from the interface between Z_{OS} and Z_{OT}. $V_S{}^+$ and $V_S{}^-$ are the incident and reflection voltage waves at the left end. $V_{T1}{}^+$ and $V_{T1}{}^-$

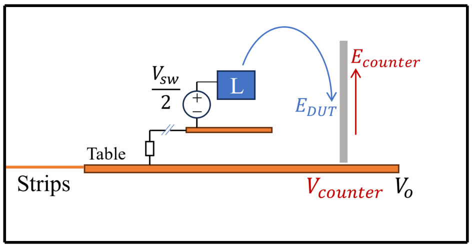

Fig. 14. Measured electric field by the monopole antenna is determined by $\mathrm{E}_{\mathrm{DUT}}$ from the inductor and $\mathrm{E}_{\mathrm{counter}}$ from the voltage $\mathrm{V}_{\mathrm{counter}}$ of the counterpoise under the monpole antenna.

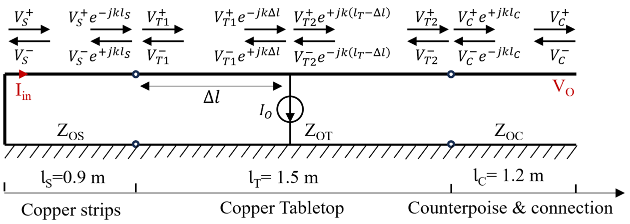

Fig. 15. Calculating the voltage along the central conductor when characterizing the system using a transmission line theory.

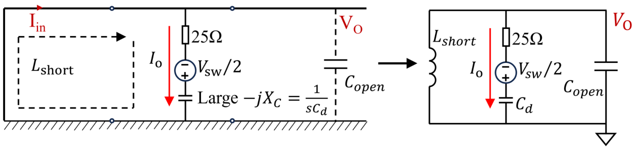

Fig. 16. Lumped circuit model used to analyze the voltage on the central conductor.

are the incident and reflection voltage waves at the interface between Z_{OS} and Z_{OT}. $V_{T2}{}^{+}$ and $V_{T2}{}^{-}$ are the incident and reflection voltage waves at the interface between Z_{OT} and Z_{OC}. $V_{C}{}^{+}$ and $V_{C}{}^{-}$ are the incident and reflection voltage waves at the right end. The voltage at the right end is V_O and the current at the left end is I_{in}. The voltage along the central conductor can be calculated based on the transmission line theory.

At low frequencies, the wavelength of the EMI noise is much bigger than the dimensions of the central conductor; therefore, a lumped circuit model in Fig. 16 can be used to analyze the voltages on the central conductor.

In Fig. 16, the displacement current I_O flows back to the $V_{SW}/2$ voltage source via chamber walls, copper strips, and copper tabletop. This current path has an inductance L_{short}. At low frequencies, the voltages $V_O = V_{\mathrm{counter}}$ and they are in phase with the voltage on the tabletop. At the same time, due to big X_C, $I_O = j0.5V_{SW}/X_C$ is 90° leading V_{SW}. Since I_O flows through L_{short}, the voltage $V_O = -j\omega L_{\mathrm{short}} I_O$ across L_{short} is, therefore, in phase with V_{SW}. C_O represents the capacitance from the counterpoise and ground connection to the chamber walls.

Since the impedance of L_{short} is proportional to frequencies and X_C is inversely proportional to frequencies, at very low frequencies, due to the large X_C and small impedance of L_{short}, V_O and V_{counter} are very small, so the measured electric field is mostly E_{DUT}. As the frequency increases, V_O, V_{counter}, and E_{counter} increase quickly. Because of this, the measured electric field E_{DUT} - E_{counter} will decrease and finally reach zero if the two are canceled. When the frequency further increases after the cancellation, the measured electric field will be dominated by -E_{counter}. So, the measured electric field will be determined by the V_{counter} of the counterpoise under the monopole antenna

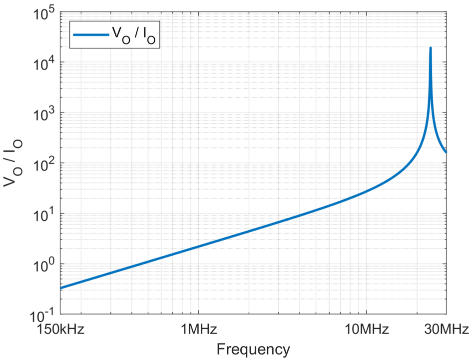

Fig. 17. Transfer impedance $\mathrm{V}_{\mathrm{O}}/\mathrm{I}_{\mathrm{O}}$ as a function of frequencies.

$$V_O = \frac{\begin{array}{c}-2jI_o\left(Z_{OC}Z_{OT}\left(Z_{OT}+Z_{OS}\right)\sin\left(k\left(\Delta l+l_S\right)\right)\right.\\ \left.+\,Z_{OC}Z_{OT}\left(Z_{OT}-Z_{OS}\right)\sin\left(k\left(\Delta l-l_S\right)\right)\right)\end{array}}{\begin{array}{c}X_1^2\cos\left(kl_{STC}\right)+X_2^2\cos\left(k\left(l_{STC}-2l_C\right)\right)\\ +X_3^2\cos\left(k\left(l_{STC}-2l_S\right)\right)+X_4^2\cos\left(k\left(l_{STC}-2l_T\right)\right)\end{array}}. \tag{17}$$

V_{counter} at high frequencies can be analyzed with the transmission line theory in Fig. 15. V_O is first solved in (17). In (17), in addition to the parameters defined in Fig. 15, l_{STC} is defined as the total length of the three transmission lines, along with the following parameters:

$$\begin{aligned} l_{STC} &= l_S + l_T + l_C \\ X_1^2 &= \left(Z_{OC}+Z_{OS}\right)\cdot Z_{OT} + Z_{OT}^2 + Z_{OC}Z_{OS} \\ X_2^2 &= \left(Z_{OC}-Z_{OS}\right)\cdot Z_{OT} - Z_{OT}^2 + Z_{OC}Z_{OS} \\ X_3^2 &= \left(Z_{OC}-Z_{OS}\right)\cdot Z_{OT} + Z_{OT}^2 - Z_{OC}Z_{OS} \\ X_4^2 &= \left(Z_{OC}+Z_{OS}\right)\cdot Z_{OT} - Z_{OT}^2 - Z_{OC}Z_{OS}. \end{aligned}$$

By plugging the parameters in Table I into (14), $Z_{OC} = 133\ \Omega$, $Z_{OT} = 51\ \Omega$, and $Z_{OS} = 65\ \Omega$. The transfer impedance Vo/I_O as a function of frequency can be plotted according to (17), as shown in Fig. 17.

It is shown in Fig. 17 that there is a spike around 24.1 MHz due to the transmission line effect on the voltage distribution along the central conductor. At low frequencies, the transfer impedance is proportional to frequencies, which agrees with the conclusion drawn from the lumped model in Fig. 16. Since there is $x_a = 0.3$ m distance between V_{counter}, the voltage where the antenna rod is located, and V_O, the voltage at the right end of the central conductor, V_{counter} can be calculated as

$$V_{\mathrm{counter}} = V_{\mathrm{O}} \cdot \cos\left(k \cdot x_a\right) \tag{18}$$

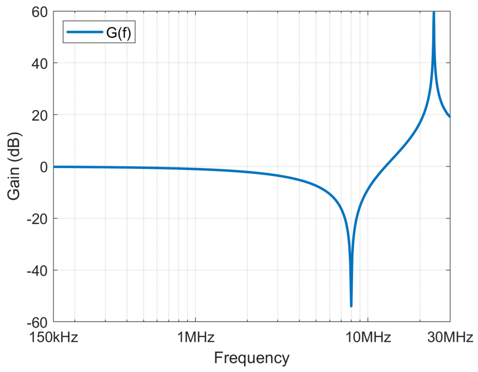

Fig. 18. Correction gain due to measurement setup.

where $k = 2\pi/\lambda$, and λ is the wavelength of the noise, which is much bigger than x_a. From (18), V_{counter} has almost the same spike frequency as the V_O.

Based on these analyses, the measured electric field is determined by E_{DUT} at low frequencies. As the frequency increases, the E_{DUT} is going to be partially canceled by E_{counter}, so the measured electric field will decrease. As the frequency further increases, the E_{DUT} will be fully canceled by E_{counter}, so the measured electric field reaches the minimal value. After the cancellation, the measured electric field will increase as the frequency increases because E_{counter} dominates, and E_{counter} increases as the frequency increases due to the transmission line effect. The measured electric field will reach a spike as V_{counter} and E_{counter} reach a spike around 24.1 MHz in Fig. 17.

Because the measured electric field is not the exact $\mathrm{E_{DUT}}$ that is supposed to measure, a correction gain (in dB) representing the impact of the measurement setup should be applied to the $\mathrm{E_{DUT}}$ to predict the finally measured electric field. A theoretical gain is derived from (E_{DUT} - E_{counter})/E_{DUT} and plotted in Fig. 18 in dB, which offers some valuable insights.

1) At low frequencies, V_O is very low, so the E field generated by the central conductor is much smaller than E_{DUT}. As a result, in Fig. 18, the gain is 0 dB.
2) As the frequency increases, V_O generates an E field with inverse direction to cancel the EUT's field, reducing the total E field measured by the monopole antenna. This phenomenon is reflected in Fig. 18 as a valley when a total cancellation happens.
3) As frequency continuously increases, V_O 's E field surpasses the EUT's E field, beginning to dominate the total E field measured by the monopole antenna. This results in an increase after the valley in Fig. 18.
4) As the frequency further increases, all four components in V_O 's denominator change significantly. By plugging the dimensions and the simulated characteristic impedance into (17), it is found that $X_1^2\cos(kl_{STC})$ has the largest amplitude and decreases fastest with frequency. When kl_{STC} slightly exceeds $\pi/4$, the denominator of V_O reaches zero. This results in a gain peak in Fig. 18.
5) After surpassing the peak frequency, the denominator of V_O is no longer zero, and the gain in Fig. 17 and Fig. 18 decreases from the peak.

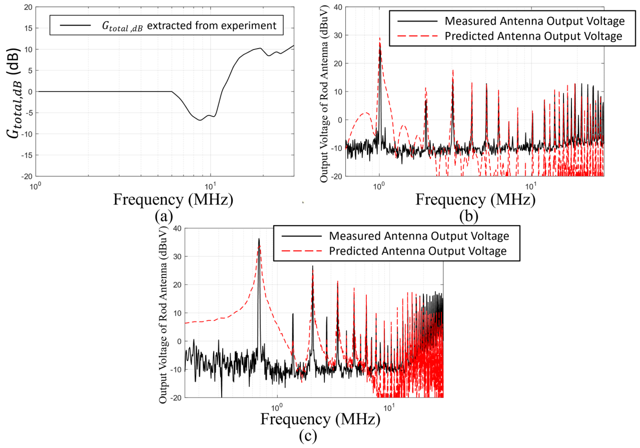

(a)

(b)

(c)

Fig. 19. (a) Experimentally extracted correction gain. (b) Spectrum of the measured output voltage of a monopole antenna for EVQ7200 with 6x6x4 mm^3 inductor matches the predicted based on the model. (c) Spectrum of the measured output voltage of a monopole antenna for EVQ2483 matches the predicted based on the developed model.

It should be pointed out that the impact of ferrite absorbers installed on the walls and the ceiling of the shielded chamber is not considered in the analysis above since the nonlinearity of the absorber will make the calculation impossible. Because of this, there is some discrepancy between the analytical results and the measured results, especially the magnitude of correction gain.

The experimentally extracted correction gain is shown in Fig. 19(a). It is similar to that in Fig. 18. Especially, the dip and peak frequencies match the analytical result in Fig. 18, which validated the developed model above.

By including the correction gain due to the measurement setup to the predicted EMI spectra of the output voltages of the monopole antenna in Figs. 9 and 10, the predicted spectra can now match the measured very well in Fig. 19(b) and (c).

B. Discussion:

1) It is worth noting that the above analysis ignores the impact of the capacitive coupling between the chamber's walls and the monopole antenna on the measurement results because it is not as important as the $\mathrm{X_C}$ between the inductor and the chamber's walls. First, the measurement setup in CISPR25 has specified $>$ 1 m distance between the monopole antenna and the chamber's walls ($>$ 1.5 m in our setup), so the capacitive coupling is very small. Second, unlike $\mathrm{X_C}$, this capacitive coupling does not influence the noise source so its impact on the noise is very small.
2) Beyond the analysis above, it is worth clarifying that the displacement current in Fig. 13, while exciting wave propagation along the central conductor, also excites wave propagation along the cable harness. The cable harness is a 1.5-m transmission line with the copper tabletop as the reference conductor. One end of the cable is connected to the reference conductor through the small impedance (25 Ω) of the LISN, and the other end is connected to the floating converter. If a resonance occurs on this cable, the resulting E field could affect the measurement result. However, the lowest resonance frequency of this cable

harness happens when $\lambda/4 = 1.5$ m, corresponding to a frequency of approximately 50 MHz, which is far beyond the concerned frequency range in this article for CISPR25. Therefore, the resonance of the cable harness is not considered in the model of this article. Nevertheless, for radiated EMI modeling studies above 30 MHz, the resonance of the cable harness should be considered.

V. CONCLUSION

This article developed and quantified a model for radiated EMI measurement with a monopole antenna up to 30 MHz. The monopole antenna's operating mechanism for electric field measurement was carefully studied and modeled. It was disclosed that the monopole antenna measures the electric field component, which is in parallel with the antenna. A model is developed to predict the output voltage of a monopole antenna based on the electric field distribution along the antenna. The impact of the measurement setup on the measured electric field was investigated and theoretically proved. A correction gain used to predict the measured electric field considering the impact of the measurement setup is derived. The analysis and the developed model have all been validated with experiments.

REFERENCES

[1] C. Nan, R. Ayyanar, and Y. Xi, "A 2.2-MHz active-clamp buck converter for automotive applications," *IEEE Trans. Power Electron.*, vol. 33, no. 1, pp. 460–472, Jan. 2018.

[2] X. Huang, Z. Liu, F. C. Lee, and Q. Li, "Characterization and enhancement of high-voltage cascode GaN devices," *IEEE Trans. Electron Devices*, vol. 62, no. 2, pp. 270–277, Feb. 2015.

[3] J. Yao, Z. Ma, Y. Lai, and S. Wang, "A survey of modeling and reduction techniques of radiated EMI in power electronics," in *Proc. IEEE Int. Joint EMC/SI/PI EMC Europe Symp.*, Raleigh, NC, USA, 2021, pp. 1081–1086.

[4] J. Yao, Y. Lai, Z. Ma, and S. Wang, "Advances in modeling and reduction of conducted and radiated EMI in non-isolated power converters," in *Proc. IEEE Appl. Power Electron. Conf. Expo.*, Phoenix, AZ, USA, 2021, pp. 2305–2312.

[5] J. Yao, M. El-Sharkh, Y. Li, Z. Ma, S. Wang, and Z. Luo, "Investigation of radiated EMI in non-isolated power converters with power cables in automotive applications," in *Proc. IEEE Energy Convers. Congr. Expo.*, Baltimore, MD, USA, 2019, pp. 6957–6964.

[6] J. Yao, Y. Lai, Z. Ma, and S. Wang, "Investigation of noise spectrum and radiated EMI in high switching frequency flyback converters," in *Proc. IEEE Appl. Power Electron. Conf. Expo.*, Phoenix, AZ, USA, 2021, pp. 2265–2270.

[7] S. Shinde et al., "Radiated EMI estimation from DC–DC converters with attached cables based on terminal equivalent circuit modeling," *IEEE Trans. Electromagn. Compat.*, vol. 60, no. 6, pp. 1769–1776, Dec. 2018.

[8] J. Yao, S. Wang, and Z. Luo, "Modeling, analysis, and reduction of radiated EMI due to the voltage across input and output cables in an automotive non-isolated power converter," *IEEE Trans. Power Electron.*, vol. 37, no. 5, pp. 5455–5465, May 2022.

[9] J. Yao, Y. Li, Z. Ma, and S. Wang, "Advances of modeling and reduction of conducted and radiated EMI in flyback converters," in *Proc. IEEE Energy Convers. Congr. Expo.*, Detroit, MI, USA, 2020, pp. 3362–3369.

[10] H. Hackl, G. Winkler, and B. Deutschmann, "Simulation of radiated emission during the design phase based on scattering parameter measurement," in *Proc. 10th Int. Workshop Electromagn. Compat. Integr. Circuits*, Edinburgh, U.K., 2015, pp. 228–231.

[11] W. T. Smith and R. K. Frazier, "Prediction of anechoic chamber radiated emissions measurements through use of empirically-derived transfer functions and laboratory common-mode current measurements," in *Proc. IEEE EMC Symp. Int. Symp. Electromagn. Compat. Symp. Rec.*, Denver, CO, USA, 1998, vol. 1, pp. 387–392.

[12] Z. Ma et al., "Radiated EMI prediction in power converters with power cables based on cable antenna voltage gain extraction," in *Proc. IEEE Int. Symp. Electromagn. Compat. Signal/Power Integrity*, Spokane, WA, USA, 2022, pp. 510–515.

[13] Jianqing Wang, O. Fujiwara, and K. Sasabe, "A simple method for predicting common-mode radiation from a cable attached to a conducting enclosure," in *Proc. Asia-Pacific Microw. Conf.*, Taipei, Taiwan, 2001, vol. 3, pp. 1119–1122.

[14] M. C. Di Piazza, A. Ragusa, G. Tine, and G. Vitale, "A model of electromagnetic radiated emissions for dual voltage automotive electrical systems," in *Proc. IEEE Int. Symp. Ind. Electron.*, Ajaccio, France, 2004, vol. 1, pp. 317–322.

[15] Z. Ma, S. Wang, H. Sheng, and S. Lakshmikanthan, "Modeling, analysis and mitigation of radiated EMI due to PCB ground impedance in a 65 W high-density active-clamp flyback converter," *IEEE Trans. Ind. Electron.*, vol. 70, no. 12, pp. 12267–12277, Dec. 2023.

[16] Y. Zhang and S. Wang, "Characterization and design of filter inductors and capacitors to suppress the radiated EMI in a power converter," in *Proc. Int. Power Electron. Conf.*, Himeji, Japan, 2022, pp. 1082–1089.

[17] M. Mehri, N. Masoumi, and J. Rashed-Mohassel, "Trace orientation function for statistical prediction of PCB radiated susceptibility and emission," *IEEE Trans. Electromagn. Compat.*, vol. 57, no. 5, pp. 1168–1178, Oct. 2015.

[18] J. Zhang, T. Lu, W. Zhang, X. Bian, and X. Cui, "Characteristics and influence factors of radiated disturbance induced by IGBT switching," *IEEE Trans. Power Electron.*, vol. 34, no. 12, pp. 11833–11842, Dec. 2019.

[19] S. Kong et al., "An investigation of electromagnetic radiated emission and interference from Multi-Coil wireless power transfer systems using resonant magnetic field coupling," *IEEE Trans. Microw. Theory Techn.*, vol. 63, no. 3, pp. 833–846, Mar. 2015.

[20] O. Aouine, C. Labarre, and F. Costa, "Measurement and modeling of the magnetic near field radiated by a buck chopper," *IEEE Trans. Electromagn. Compat.*, vol. 50, no. 2, pp. 445–449, May 2008.

[21] Y. Lai, J. Yao, S. Wang, Z. Luo, and Y. Li, "Electric near Field emission from a 1 MHz power converter for electric vehicles," in *Proc. IEEE Energy Convers. Congr. Expo.*, Vancouver, BC, Canada, 2021, pp. 2881–2887.

[22] M. El-Sharkh, S. Wang, and B. Zhang, "Investigation and reduction of near electric field emitted from a power helical inductor," in *Proc. IEEE Energy Convers. Congr. Expo.*, Detroit, MI, USA, 2020, pp. 5890–5897.

[23] Y. Lai, Y. Yang, S. Wang, and Z. Luo, "A novel low-frequency radiated emissions prediction technique for the inductor of a non-isolated power converter," in *Proc. IEEE Energy Convers. Congr. Expo.*, Detroit, MI, USA, 2022, pp. 1–8.

[24] J. Song, H. T. Hui, and Z. W. Sim, "Investigation of measurement uncertainties and errors in a radiated emission test system," *IEEE Trans. Electromagn. Compat.*, vol. 57, no. 2, pp. 158–163, Apr. 2015.

[25] N. Bondarenko et al., "A measurement-based model of the electromagnetic emissions from a power inverter," *IEEE Trans. Power Electron.*, vol. 30, no. 10, pp. 5522–5531, Oct. 2015.

[26] C. Qiang and L. Yinghua, "The influence of different measurement antennas on the radiated emission measurement," in *Proc. Int. Conf. Electron., Commun. Control*, Ningbo, China, 2011, pp. 4010–4014.

[27] J. Lee, K. Jung, and S. Park, "Simulation of radiated emissions from a low voltage BLDC motor," in *Proc. Int. Symp. Antennas Propag.*, Busan, South Korea, 2018, pp. 1–2.

[28] I. Oganezova, R. Kado, B. Khvitia, A. Gheonjian, and R. Jobava, "Simulation of conductive and radiated emissions from a wiper motor according to CISPR 25 standard," in *Proc. IEEE Int. Symp. Electromagn. Compat.*, Dresden, Germany, 2015, pp. 963–968.

[29] B. A. Austin and A. P. C. Fourie, "Characteristics of the wire biconical antenna used for EMC measurements," *IEEE Trans. Electromagn. Compat.*, vol. 33, no. 3, pp. 179–187, Aug. 1991.

[30] L. Turnbull, "The Groundplane Resonance – problems with radiated emissions measurements below 30 MHz," in *Proc. Automot. EMC Conf.*, Newbury, U.K., 2007, vol. 16, pp. 1–13.

[31] D. Warkentin, A. Wang, and W. Crunkhorn, "Shielded enclosure accuracy improvements for MIL-STD-461E radiated emissions measurements," in *Proc. Int. Symp. Electromagn. Compat.*, Chicago, IL, USA, 2005, vol. 2, pp. 404–409.

[32] C. W. Fanning, "Improving monopole radiated emission measurement accuracy; RF chamber influences, antenna height and counterpoise grounding (CISPR 25 & MIL-STD-461E vs MIL-STD-461F)," in *Proc. IEEE Int. Symp. Electromagn. Compat.*, Austin, TX, USA, 2009, pp. 103–118.

[33] H. W. Gaul, “Electromagnetic modeling and measurements of the 104 cm rod and biconical antenna for radiated emissions testing below 30 MHz,” in *Proc. IEEE Int. Symp. Electromagn. Compat.*, Denver, CO, USA, 2013, pp. 434–438.

Yirui Yang (Student Member, IEEE) received the B.S. degree in electrical engineering and the M.S. degree in power electronics from Shanghai Jiao Tong University, Shanghai, China, in 2017 and 2020, respectively. He is currently working toward the Ph.D. degree in electrical and computer engineering with the University of Florida, Gainesville, FL, USA.

His research interests include power electronics EMI/EMC, magnetic components, wireless power transfer, cyber security, and hardware security. He has authored and coauthored more than 21 IEEE journal and conference papers since 2022.

Yanwen Lai (Student Member, IEEE) received the bachelor’s degree in electric engineering and automation from the South China University of Technology, Guangzhou, China, in 2016, and the master’s degree in electrical and computer engineering from the University of Florida, Gainesville, FL, USA, in 2018. He is currently working toward the Ph.D. degree in electrical and computer engineering from the University of Florida, Gainesville, FL, USA.

His research interests include power electronics EMI/EMC and magnetic components.

Shuo Wang (Fellow, IEEE) received the Ph.D. degree in electrical engineering from Virginia Tech, Blacksburg, VA, USA, in 2005.

He is currently a Full Professor with the Department of Electrical and Computer Engineering, University of Florida, Gainesville, FL, USA. He has authored or coauthored more than 250 IEEE journal and conference papers and holds more than 30 pending/issued U.S./international patents.

Dr. Wang was the recipient of the Best Transaction Paper Award from the IEEE Power Electronics Society in 2006 and two William M. Portnoy Awards for the papers published in the IEEE Industry Applications Society in 2004 and 2012, respectively, recipient of the Distinguished Paper Award from 2022 IEEE Symposium on Security and Privacy, and was also the recipient of the prestigious National Science Foundation CAREER Award, in 2012. He is an Associate Editor for IEEE TRANSACTIONS ON INDUSTRY APPLICATIONS and IEEE TRANSACTIONS ON ELECTROMAGNETIC COMPATIBILITY, as well as the Guest Editor of IEEE Transactions on Power Electronics. He is the Chair of Power Electronics EMI/EMC Special Committee of IEEE EMC Society and an Instructor of IEEE Clayton Paul Global University. He was a Technical Program Co-Chair of the IEEE 2014 International Electric Vehicle Conference.

Zheng Luo received the M.S. degree in electrical engineering from Virginia Tech, Blacksburg, VA, USA, in 2008.

He is currently a Sr. Manager with Monolithic Power Systems, San Jose, CA. He holds more than 20 US/international patents. His research interests include power electronic circuits, control, and power management ICs.